

Dynamic Molding Deposition: The additive manufacturing in partially ordered system

Christophe Marquette (✉ christophe.marquette@univ-lyon1.fr)

3d.FAB - Université Lyon1

Edwin-Joffrey Courtial

3d.FAB - Université Lyon1

Arthur Colly

3d.FAB - Université Lyon1

Article

Keywords: Additive manufacturing, Dynamic Molding Deposition, partially ordered system

Posted Date: April 15th, 2021

DOI: <https://doi.org/10.21203/rs.3.rs-354619/v1>

License: © ⓘ This work is licensed under a Creative Commons Attribution 4.0 International License.

[Read Full License](#)

Dynamic Molding Deposition: The additive manufacturing in partially ordered system

Authors: E.-J. Courtial¹, A. Colly¹, C.A. Marquette^{1*}

Affiliations:

5 ¹ 3d.FAB, Univ Lyon, Université Lyon1, CNRS, INSA, CPE-Lyon, ICBMS, UMR 5246, 43, Bd du 11 Novembre 1918, 69622 Villeurbanne Cedex, France

*Correspondence to: christophe.marquette@univ-lyon1.fr

Abstract:

Additive manufacturing (AM) is now identified as a powerful bundle of fabrication techniques. Limitations were identified to be mostly related to the availability of reformulated materials compatible with existing AM technologies. What if we were able to dynamically generate sacrificial molds with unlimited architectures and material composition? We have discovered such a process, called Dynamic Molding Deposition (DMD) in partially ordered powder system and demonstrated its capacity to produce highly complex objects with 100 μm resolution, without any building plate or support structures. The DMD compatible materials were shown to be almost infinite, from low to high viscosity, from thermoplastic to elastomers. Our process enables us to build unexpected composite objects made up of injection material and powder grains from the dynamic mold. This feature opens the path to a complete new field of research and applications.

20 **One Sentence Summary:** Dynamic molding, the missing link between molding and additive manufacturing, will enable the production of high technicality materials and composites.

Main Text:

Additive manufacturing is now identified by academics and industries as a powerful bundle of fabrication techniques enabling the rapid, free-form, sometime low-cost and surely straightforward production of prototypes and functional parts (1). Applications are widespread from aerospace to biology, from energy to food but the processes hidden behind the machines are always focused on physico-chemical reactions enabling liquid-solid transition of the printed material (polymerization, recrystallization, gelation...) (2, 3). This phase transition on the one hand permits the creation of self-standing complex architectures but on the other hand usually demands specific re-formulation of the initial manufacturing material (4, 5). The consequence being here that materials not compatible with re-formulation are automatically excluded of the additive manufacturing world and remain then in the molding/injection/thermoforming domain.

What if we were able to dynamically generate sacrificial molds with unlimited architectures? This might be the innovation the community was waiting, the missing link between molding and extrusion-based additive manufacturing. Such a manufacturing process, able to print in three dimensions all materials regardless of their chemistry, would provide a breakthrough in the field and complement all existing additive manufacturing methods.

Attempts to such progress have been made in the last 5 years with the tremendous successes of the Freeform Reversible Embedding of Suspended Hydrogels (FRESH) (6), the Embedded 3D Printing (EMB3D) (7), the PICSIMA technique using a 2-part A/B silicone where the part A-silicone catalyst-cross-linker is extruded into a bath of part B-silicone (8), the Sacrificial Writing Into Functional Tissue (SWIFT) (9) and the more recent in-bath print and cure (IBPC) (10), allowing the printing of low static yield stress materials (11) within a suspending gel environment. It was then possible to print some classical viscoelastic materials (silicones and hydrogels) without

re-formulation. Nevertheless the application range of these gel-based embedded techniques remained restricted by the necessary chemical and rheological compatibility of the printed material with the suspending environment (12).

In a bid to solve these incompatibilities and propose a universal additive manufacturing process, we discovered the Dynamic Molding Deposition (DMD), allowing us to produce free-form geometries through extrusion-based additive manufacturing of a wide range of injectable materials in a partially ordered system of solid granular material (13). The DMD approach is characterized by several advantages such as the absence of support or building table, the possibility to process materials regardless their viscosity and chemistry, the potentiality to create new hybrids materials through the process (porosity, composites, gradient properties and surface modification). **Figure 1-A** presents the DMD conceptual approach. The DMD process assumes that all manufacturing materials can be 3D printed when the printing environment fulfil at least 3 functions: 1) SUPPORTING the deposited material (just like when using suspended hydrogels), 2) COMPRESSION of the deposited material in a filament-like structure and 3) SELF-REPAIRING itself after disruption by the printing head movement. Thus, using these three properties, low and high viscosity materials shall be 3D shaped without collapsing, the system being able to counterbalance gravity deleterious effects. In a similar way, slow and rapid phase changing constituents might be used since the produced dynamic mold shall be stable long enough to enable cross-linking, polymerization or recrystallization of the material.

In the DMD approach, the printing environment is composed of a dynamic mold (a partially ordered powder system) (13). Its flowability properties (14), density and grain shape bringing altogether the necessary properties to the environment. **Figure 1-B** presents the positioning of the different DMD environments within an ability diagram (Compressibility vs Mean diameter (D50)).

As can be seen, a large range of powder compositions, from organic to mineral (see **Table S1** and **S3**), from water soluble to insoluble, can be used, bringing infinite material-powder association possibilities. The obtained new composites at reach being also infinite. Some molds were also unreachable (cement for example), mainly because of the powder grain to grain electrostatic interaction (at low diameter) and cohesion (at high compressibility) (15).

The behavior of the deposited material within the dynamic mold during 3D deposition was partially simulated using Computational Fluid Dynamics (CFD) modelling (16). The supporting and containment properties of the powder were thus investigated at the powder grain level. A Volume Of Fluid (VOF (17)) method for two-phases flow combined with dynamic mesh capabilities based on overset mesh technics were used to simulate a viscoelastic material deposition within a dynamic mold. The VOF model captures the free surface of the viscoelastic fluid and takes into account interfacial tension effects. Overset mesh technics (18) were used to move the extrusion nozzle over the dynamic mold. **Figure 1-C** depicts the simulated deposition. As can be seen, the developed simulation is able to describe material flow through the grains but also the potential material transfer to other layers. It highlights also the interaction between injected material and previously printed filaments (**Figure S2**, **Movie S1** and **Movie S2**). Clear proofs of the ability of the dynamic mold to maintain the printed material in a controlled geometry were here numerically obtained. The DMD resolution, based on these simulations, shall be in the order of magnitude of the powder grain size. The best results being obtained using ~100 μm diameter grains, an average resolution of 100 μm is expected and was validated experimentally (**Figure S4**). The simulation was also of great help understanding the DMD behaviors of materials with different viscosities, which leads to different powder integration within the final composite (**Table S2**).

We modified two 3D printing systems to produce two experimental set-ups used in this work (**Figure 1-D**). A 3-axis (Cartesian) and a 6-axis 3D printers were thus hybridized with a thermo-regulated dynamic mold and a deposition head composed of a microdosing system (vipro-HEAD 5, ViscoTec, Germany) or a pressure-controlled system, respectively. Since the material used for the additive manufacturing using DMD can be theoretically of very low viscosity, the strategy was here to implement a system handling from 10^{-3} to 10^6 Pa.s viscosity. An interesting example of the DMD versatility is the printing of the polycaprolactone (PCL) (**Figure 2-B**) which was simply dynamically molded in a 100°C heated glass beads dynamic mold. At this temperature, PCL viscosity is closed to 10^{-1} Pa.s and the polymer is easily extruded but also kept liquid within its dynamic mold. Once the manufacturing completed, the DMD environment is then slowly cooled down until solidification at room temperature. The obtained objects were of acceptable fidelity and made up of a new organic-inorganic composite material. Achieving these composites is a particular case of the DMD process where powder grains are trapped between the injected material layers (**Figure S5**).

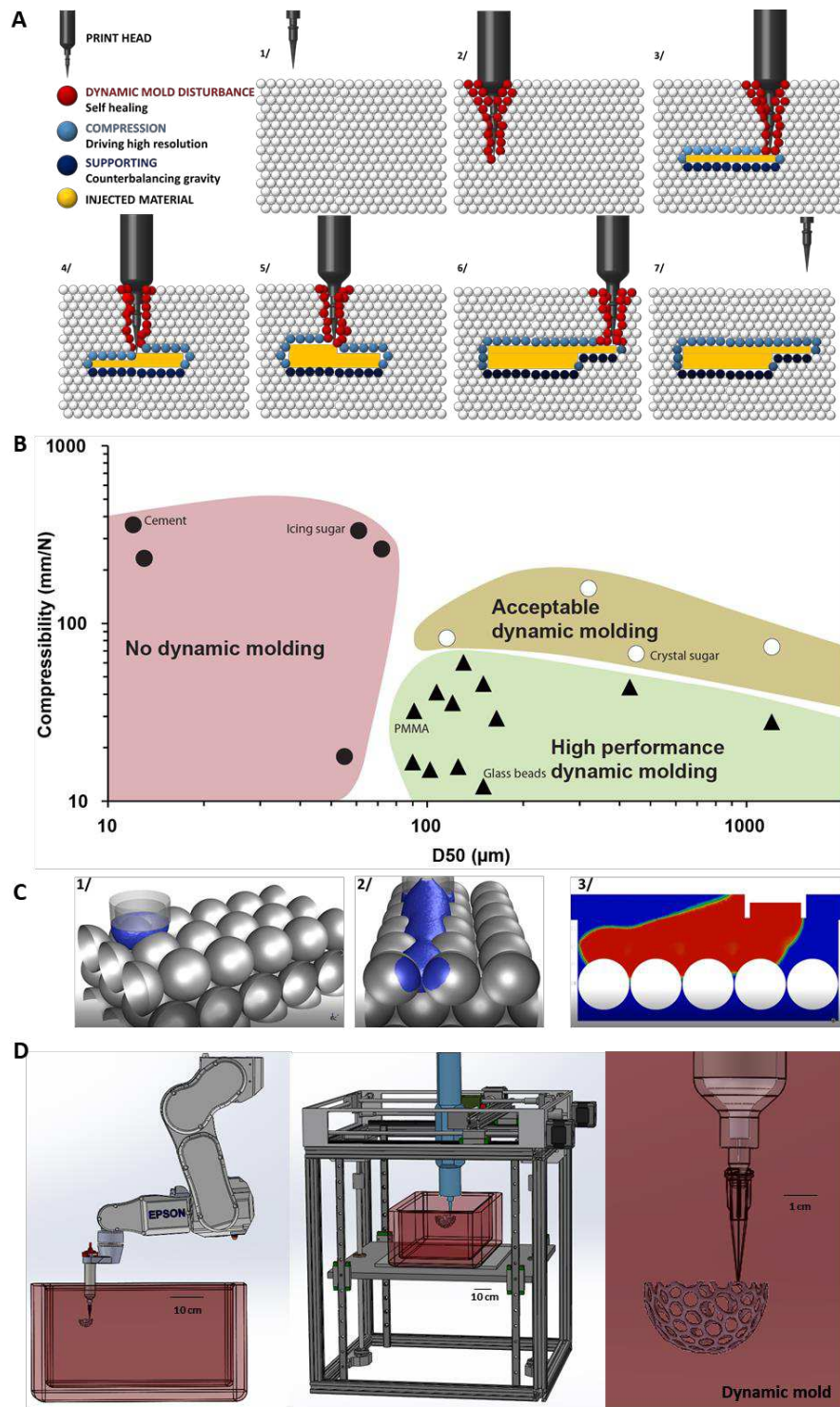


FIG.1: Dynamic Molding Deposition. (A) Conceptual approach of the DMD showing the different behaviors of the dynamic mold (composite variant process can be found in **Figure S4**). Material printing sequence of two layers, from 1/ to 7/. (B) Selection mapping of the dynamic mold according to compressibility and particle diameter. (C) Computational Fluid Dynamics (CFD) modelling simulation of SYLGARD™ 567 DMD within silica beads. 1/ at t=0, 2/ at t= 8.5 msec, 3/ profile of the deposited material. (D) Modified 3D printers, 6-axis robotic (left) and 3-axis printer (center). Closer view of the DMD of a voroid sphere without building plate or support structure.

The ability to produce freeform geometries without considering building plate positioning or supporting structures offers multiple advantages compared to classical additive manufacturing methods.

Figure 2 depicts a series of complex voroid structures, known to be the most difficult 3D structures to be produced (19, 20), even with 3D printing-optimized classical polymer materials such as polylactic acid (PLA) or acrylonitrile butadiene styrene (ABS). In order to challenge DMD, we decided to manufacture these complex objects (**Table S2**) with challenging materials such as silicone elastomers of low (10^{-1} Pa.s) and high viscosity (10^4 Pa.s), and characterized by very long reticulation time (pot life > 24H).

To illustrate the inherent challenges of such 3D printing, a predictive algorithm (FingerMap (21)) was used to visualize the non-printable parts of the different objects according to the rheological properties of the material (here example of AMSil™ 20101). In this predictive approach, our software voxelizes the STL files and uses four inputs (the mass density and the static yield stress (τ_y^s) of the printed material, the mass/surface ratio of each voxel and the expected resolution) to generate a comprehensive map of printability (**Figure 2-B**) together with a 3D visualization (**Figure 2-B insert**). Briefly, the green plane of the FingerMap defines the limit of printability and all blue scattered dots above this plane are non-printable voxels. This information is translated in the 3D visualization where green parts are printable and red parts of the STL are not printable. Obviously, 3D printing of these objects, in non-suspended conditions and using the selected silicone material, is impossible. Nevertheless, when looking at the DMD-based prints of these STLs (**Figure 2-C**), overhanging and disconnected parts were easily produced. This is the strength of the DMD process and the uniqueness of the approach which was pushed forward with a wide range of highly complex structures (**Figure 3** and FingerMap printability evaluation in **Table S4**).

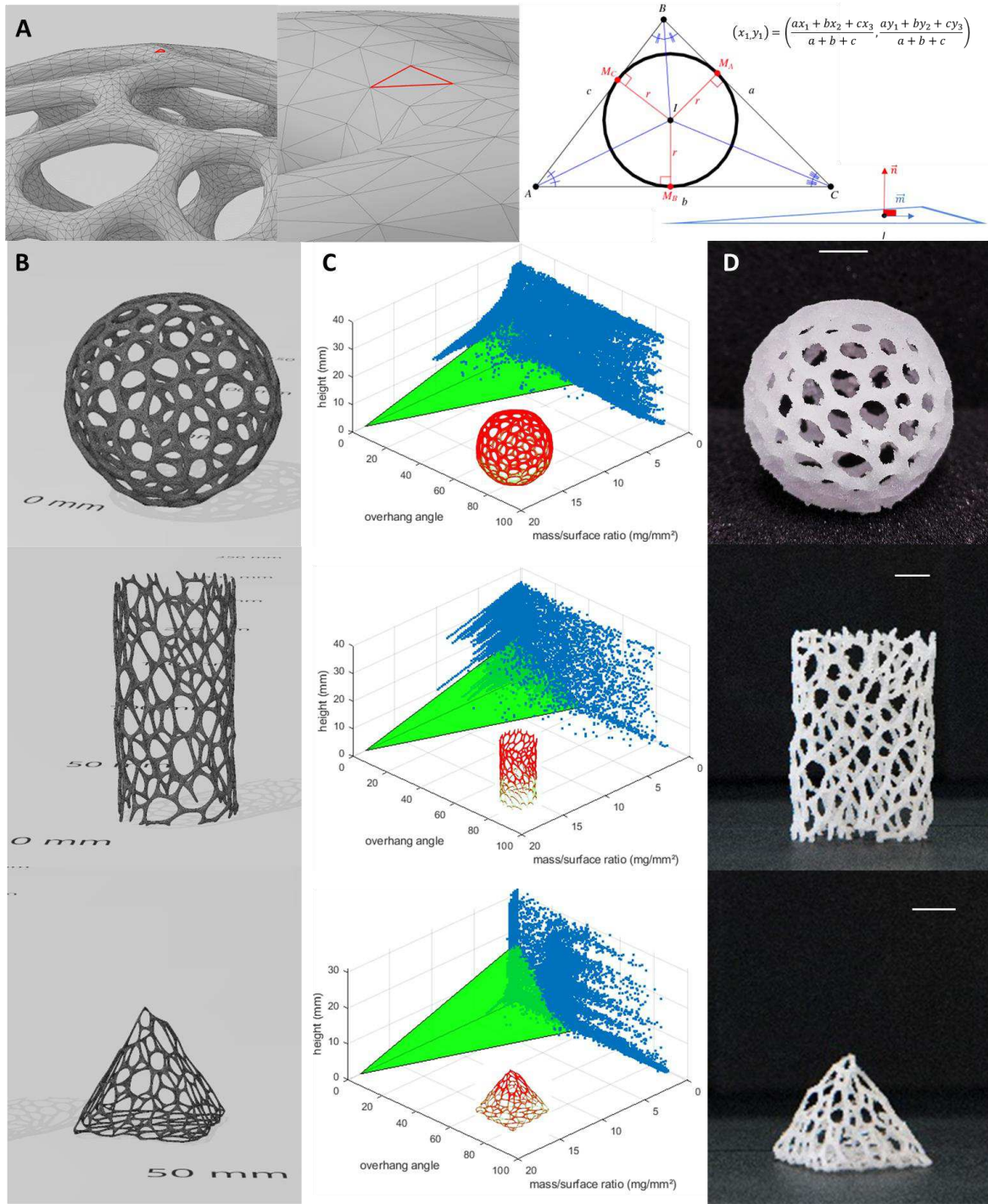


FIG.2: Voroids printability simulation using FingerMap. (A) Each triangle of STL file is described through incenter by FingerMap tool. The incenter I is the center of the incircle for a polygon or insphere for a polyhedron. For a triangle with Cartesian vertices (x_1, y_1) , (x_2, y_2) , (x_3, y_3) , the Cartesian coordinates of the incenter are given by the presented equation. Then, normal vector (red) is defined for each triangle of STL file from incenter corresponding to $\vec{n} \cdot \vec{m} = 0$. (B) STL file of the studied voroids. (C) FingerMap and simulation and the experimental 3D print (insert) for each STL. The green volume represents the printability of the material. Each blue dot represents a voxel. In the prediction, red voxels represent not-printable area while green voxels represent printable area. (C) Voroids obtained through DMD using monocomponent room temperature vulcanization alkoxy silicone (AMSil™ 20101) within glass beads.

This exceptional property also brings new engineering capabilities where objects can be formed through multiple directions within the dynamic mold. A first example of this capacity has been the simultaneous production of multiple H2 tensile bars with variable angle with respect to normal (from 0 to 90°) or at different deepness within the dynamic mold (from 40 to 80 mm). The mechanical properties (**Figure 4-A**) of these tensile bars were strongly conserved (Young's modulus and fracture strains) with a minimized effect of the printing angle upon the expected inter-layer failure (lowering of the fracture strain) (22).

A second example is the capacity of producing multi-material complex objects, represented in **Figure 3-C**, by the inclusion of one voroid sphere in a second voroid sphere, each one being molded with a different material.

As a final example of the extreme freeform capability of DMD, we rendered a highly complex physiological shape composed of a mitral valve, eight chordae tendineae and two medial papillary muscles (**Figure 3-D**). Here, the printing sequence was composed of three different steps, i) a planar layer by layer deposition of the mitral valve, ii) a 6-axis path-based multidirectional deposition of the eight chordae tendineae and iii) a final planar layer by layer deposition of the two medial papillary muscles. These three sequences were supposed to bring even more complexity to the printing process since multiple objects shall be connected within the dynamic mold with enough cohesion. Here, it is worth to point out that the 8 chordae tendineae were printed as single 1 mm filaments, positioned between the two other sequences but still cohesive with the other objects. **Figure 3-D** presents the silicone final object obtained using a glass beads dynamic mold. As can be seen, all the parts were cohesive with a surface quality and a fidelity toward the initial STL file. To document this fidelity, dimensional measurements of the printed object were

performed and compared to the initial STL (printing fidelity: 97.49%, **Table S5**). Another example of the power of the DMD to enable the production of complex structures is depicted in **Figure 4-E** where a lattice structure, characterized by a hyper-viscoelastic behavior was obtained using path-based 6-axis deposition. In this configuration, the object was fully designed as 6-axis paths and the final rendering of the lattice with its deformability are presented in **Movie S3** and **Movie S4**. From uniaxial compression tests, an expected clear non-linear stress-strain relationship was identified (load cure). Thus, hysteresis between load and unload steps represents the configurational free energy of the viscoelastic solid and characterizes the non-equilibrium state. The object mechanical properties can then be described by a hyper-viscoelastic behavior using the following constitutive equation (23):

$$\Psi(\mathbf{C}, \mathbf{\Gamma}_1, \dots, \mathbf{\Gamma}_m) = \Psi_{iso}^{\infty}(\bar{\mathbf{C}}) + \sum_{\alpha=1}^m \Upsilon_{\alpha}(\bar{\mathbf{C}}, \mathbf{\Gamma}_{\alpha}) \quad (1)$$

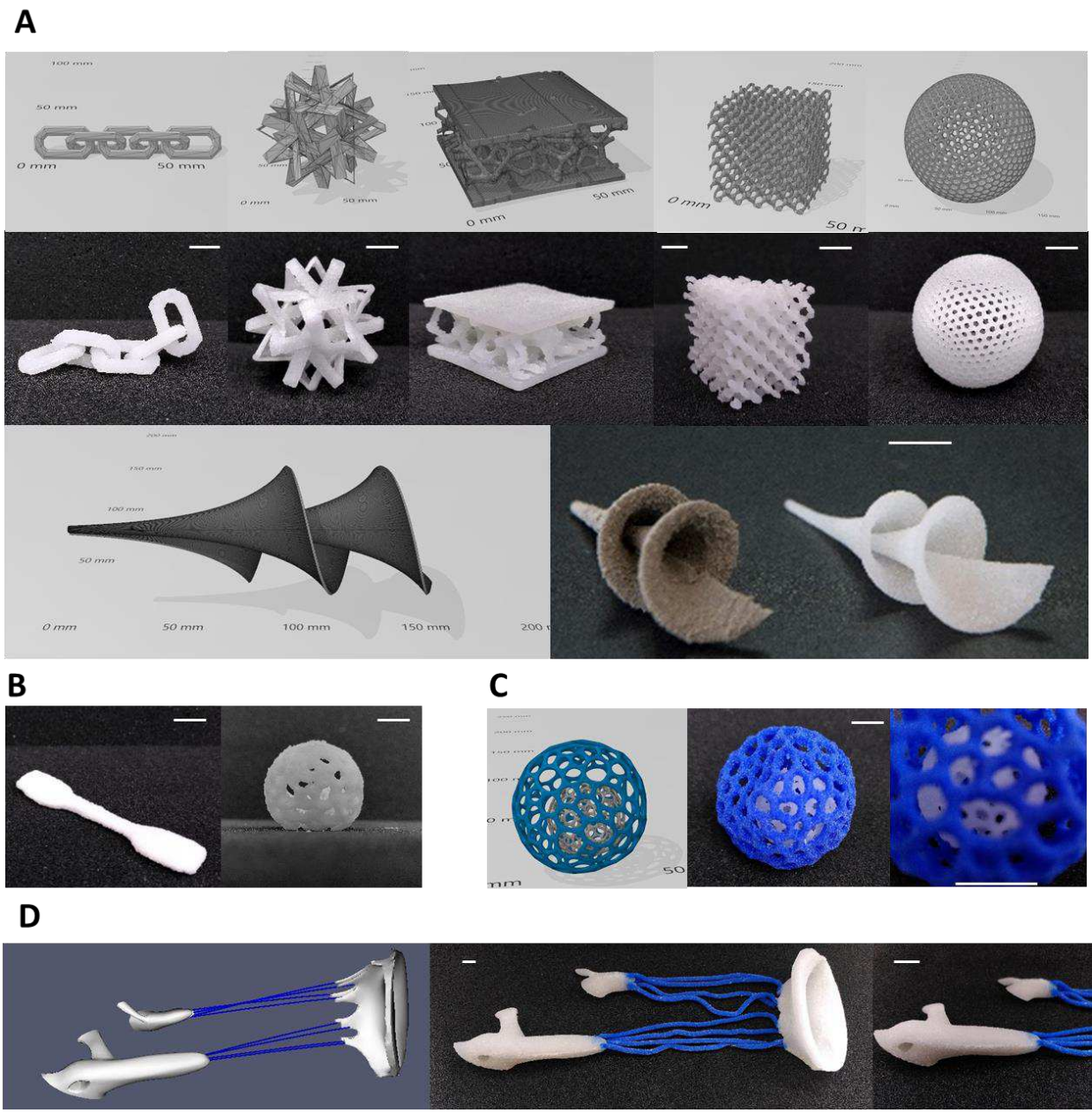


FIG. 3: Multiple examples of complex objects produced by DMD. (A) A series of highly complex STL geometries (top) and produced objects (bottom) obtained using monocomponent room temperature vulcanization alkoxy silicone (AMSi™ 20101) within glass beads (white parts) or cenospheres (grey parts) dynamic molds. (B) Polycaprolactone thermoplastic H2 tensile bar and voroid sphere obtained using DMD in glass beads. (C) Voroid ball within voroid ball STL (left) and object produced using two colored alkoxy silicone (AMSi™ 20101). (D) DMD enabling production of complex shapes through the merging of 3-axis and 6-axis multidirectional deposition within a single object. Left: STL multiple files and multidirectional trajectories (blue lines). Center: the DMD enabled object. Right: a closer view of the cohesion between Cartesian print and multidirectional deposition. Scale bars are 1 cm.

5

10

DMD has been developed to fulfil the gap between molding and 3D printing, but an additional extraordinary feature of the technique is its ability to produce, directly during fabrication, composites of various composition. **Figure 4-C** and **4-D** depict multiple examples of such composites together with their surface characterization and mechanical properties. Interestingly, the mechanical properties of the obtained composites were also controlled by the dynamic mold composition. Indeed, for a specific deposited material (here AMSil™ 20101, Elkem Silicones, France), changing the mold from sacrificial PMMA powder to glass, silica and then sugar, leads to a constant increase of the Young's modulus and a variation of the material resistance to tension. Applications of this composite material direct freeform fabrication are numerous, from fire proofing (25) to thermal conductivity (26), antibacterial properties (27) and even flexible gamma shielding (28), to name a few.

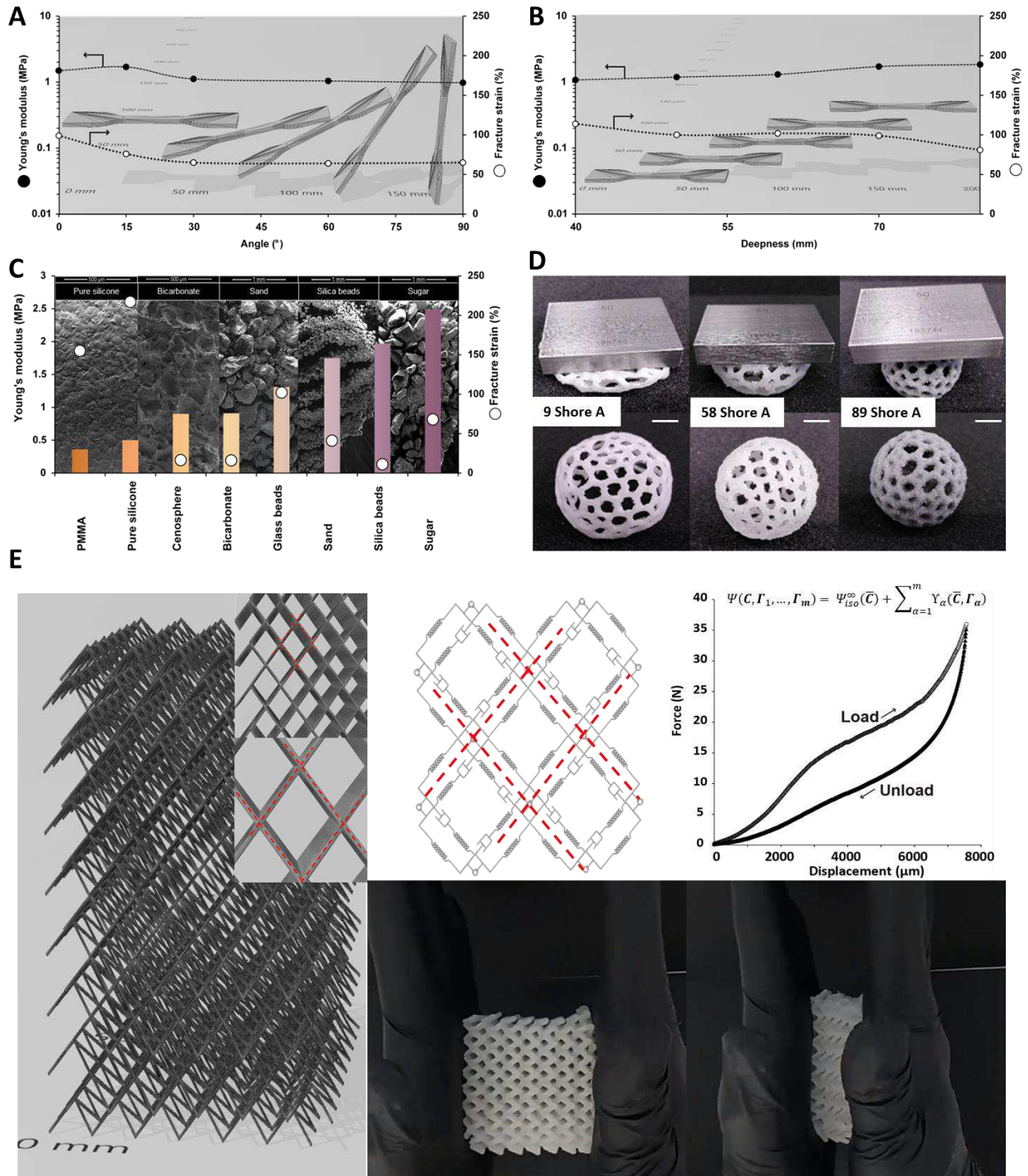


FIG. 4: DMD produced objects and composites characterizations. (A) Mechanical properties (Young's modulus and Fracture strain) of DMD silicone objects positioned at different angles within a single glass beads mold (mean error for all measurements 5%). (B) Mechanical properties (Young's modulus and Fracture strain) of DMD silicone objects positioned at different deepness within a single glass beads mold (mean error for all measurements 5%). (C) Topographic analysis (electronic microscopy images in background) and mechanical properties (Young's modulus and Fracture strain) of multiple silicone (AMSil™ 20101) composites (mean error for all measurements 5%). (D) Demonstration of the capacity of the DMD to produce a wide range of stiffness (testing weight: 50g). Left: AMSil™ 20101 obtained in sacrificial PMMA powder. Center: AMSil™ 20101 obtained in glass beads powder. Right: SYLGARD™ 567 obtained in glass beads powder. (E)

Lattice structure characterized by a non-linear hyper-viscoelastic behavior and obtained using path-based 6-axis deposition strategy. Mechanical model representative of the non-linear hyper-viscoelastic. Load/unload compression curve and constitutive equation.

5

References and Notes:

1. O. Abdulhameed, A. Al-Ahmari, W. Ameen, S. H. Mian, Additive manufacturing: Challenges, trends, and applications. *Advances in Mechanical Engineering* **11**, 1687814018822880 (2019/02/01, 2019).
- 5 2. W. Yu, X. Wang, E. Ferraris, J. Zhang, Melt crystallization of PLA/Talc in fused filament fabrication. *Mater Design* **182**, 108013 (2019/11/15/, 2019).
3. E. J. Courtial *et al.*, Silicone rheological behavior modification for 3D printing: Evaluation of yield stress impact on printed object properties. *Additive Manufacturing* **28**, 50 (Aug, 2019).
- 10 4. S. C. Ligon, R. Liska, J. Stampfl, M. Gurr, R. Mülhaupt, Polymers for 3D Printing and Customized Additive Manufacturing. *Chemical Reviews* **117**, 10212 (2017/08/09, 2017).
5. X. Wang, M. Jiang, Z. Zhou, J. Gou, D. Hui, 3D printing of polymer matrix composites: A review and prospective. *Composites Part B: Engineering* **110**, 442 (2017/02/01/, 2017).
- 15 6. T. Hinton *et al.*, Three-dimensional printing of complex biological structures by freeform reversible embedding of suspended hydrogels. *Sci Adv* **1**, e1500758 (10/23, 2015).
7. A. K. Grosskopf *et al.*, Viscoplastic Matrix Materials for Embedded 3D Printing. *Acs Applied Materials & Interfaces* **10**, 23353 (Jul 11, 2018).
8. T. Fripp, N. Frewer, L. Green. (European, 2013), vol. EP3060380B1.
- 20 9. M. A. Skylar-Scott *et al.*, Biomanufacturing of organ-specific tissues with high cellular density and embedded vascular channels. *Sci Adv* **5**, eaaw2459 (2019).
10. M. Mahmoudi, S. R. Burlison, S. Moreno, M. Minary-Jolandan, Additive-Free and Support-Free 3D Printing of Thermosetting Polymers with Isotropic Mechanical Properties. *ACS Applied Materials & Interfaces*, (2021/01/21, 2021).
- 25 11. J. Zhao, N. He, A mini-review of embedded 3D printing: supporting media and strategies. *Journal of Materials Chemistry B* **8**, 10474 (2020).
12. C. S. O'Bryan *et al.*, Three-dimensional printing with sacrificial materials for soft matter manufacturing. *Mrs Bull* **42**, 571 (2017).
13. J. Duran, in *Sands, Powders, and Grains*. (Springer-Verlag New York, 2000).
- 30 14. M. M. de Campos, M. D. Ferreira, A Comparative Analysis of the Flow Properties between Two Alumina-Based Dry Powders. *Adv Mater Sci Eng* **2013**, (2013).
15. J. P. K. Seville, C. D. Willett, P. C. Knight, Interparticle forces in fluidisation: a review. *Powder Technol.* **113**, 261 (Dec 6, 2000).

16. H. H. Hu, in *Fluid Mechanics (Fifth Edition)*, P. K. Kundu, I. M. Cohen, D. R. Dowling, Eds. (Academic Press, Boston, 2012), pp. 421-472.
17. N. D. Katopodes, in *Free-Surface Flow*, N. D. Katopodes, Ed. (Butterworth-Heinemann, 2019), pp. 766-802.
- 5 18. A. Berton, F. D’Orrico, M. Sideri, Overset grids for fluid dynamics analysis of internal combustion engines. *Energy Procedia* **126**, 979 (2017/09/01/, 2017).
19. N. Shahrubudin, P. Koshy, J. Alipal, M. H. A. Kadir, T. C. Lee, Challenges of 3D printing technology for manufacturing biomedical products: A case study of Malaysian manufacturing firms. *Heliyon* **6**, e03734 (2020).
- 10 20. M. Livesu, S. Ellero, J. Martínez, S. Lefebvre, M. Attene, From 3D models to 3D prints: an overview of the processing pipeline. *Computer Graphics Forum* **36**, 537 (2017/05/01, 2017).
21. A. Lopez, C. A. Marquette, E.-J. Courtial, FingerMap: a new approach to predict soft material 3D objects printability. *Progress in Additive Manufacturing*, (2020/07/08, 2020).
- 15 22. T. Yao *et al.*, Tensile failure strength and separation angle of FDM 3D printing PLA material: Experimental and theoretical analyses. *Composites Part B: Engineering* **188**, 107894 (2020/05/01/, 2020).
23. Wiley, Ed., *Nonlinear Solid Mechanics: A Continuum Approach for Engineering*, (2000).
24. R. W. Ogden, R. Hill, Large deformation isotropic elasticity - on the correlation of theory and experiment for incompressible rubberlike solids. *Proceedings of the Royal Society of London. A. Mathematical and Physical Sciences* **326**, 565 (1972).
- 20 25. Y. Kim *et al.*, Valorization of fly ash as a harmless flame retardant via carbonation treatment for enhanced fire-proofing performance and mechanical properties of silicone composites. *J Hazard Mater* **404**, 124202 (Oct 8, 2020).
- 25 26. J. T. Wertz, J. P. Kuczynski, D. J. Boday, Thermally Conductive-Silicone Composites with Thermally Reversible Cross-links. *ACS Appl Mater Interfaces* **8**, 13669 (Jun 8, 2016).
27. X. Yu *et al.*, Preparation of experimental resin composites with an anti-adhesion effect against *S. mutans* using branched silicone methacrylate. *Journal of the mechanical behavior of biomedical materials* **101**, 103414 (Jan, 2020).
- 30 28. B. Ahmed, G. B. Shah, A. H. Malik, Aurangzeb, M. Rizwan, Gamma-ray shielding characteristics of flexible silicone tungsten composites. *Appl. Radiat. Isot.* **155**, 108901 (Jan, 2020).

Acknowledgments: The authors acknowledge CFD Numerics for their help in solving the modelling of the DMD. The authors acknowledge ELKEM Silicones France for supplying silicone materials and technical support in characterizing them. **Author contributions:** C.M. and E-J.C. designed the research and provide overall direction; E-J.C. and A.C. performed material and powder characterizations; E-J.C. supervised the DMD modelling work; C.M. developed the 6-axis robotic arm approach; all authors contributed to analysis and to writing and refining the manuscript. **Competing interests:** The authors are inventors on a world patent application related to this work (WO2020109745A1). All authors declare that they have no other conflict of interest. **Data and materials availability:** All data is available in the main text or the supplementary materials.

Supplementary Materials:

Materials and Methods

Figures S1-S4

Tables S1-S5

Movies S1-S7

References (1-26)

Supplementary Materials for

Dynamic Molding Deposition additive manufacturing in partially ordered system

5 E.-J. Courtial, A. Colly, C.A. Marquette.

Correspondence to: christophe.marquette@univ-lyon1.fr

10 **This PDF file includes:**

Materials and Methods

Supplementary Text

Figs. S1 to S4

15 Tables S1 to S5

Captions for Movies S1 to S7

Other Supplementary Materials for this manuscript include the following:

20 Movies S1 to S7

Materials and Methods

Materials

5 **Table S1:** list of powder used as Dynamic Mold.

DMD powder	Source
Cement	Axton, Leroy Merlin, France
Icing sugar	Daddy, France
Flour	Francine®, France
Glass beads #1	OTS-Store, Germany
Cornflour	Maïzena®, France
Laundry powder	L'arbre vert, France
Ground coffee (small)	Nescafé® FR, France
Ground coffee (coarse)	Nescafé® FR, France
Sugar	Carrefour, France
Sand	Natur déco ®, Leroy Merlin, France
Cenosphere	Elkem, Norway
PMMA	Sigma Aldrich, France
Bicarbonate	La baleine, France
Fine salt	Carrefour, France
Silica beads	Supelco® analytical, Sigma Aldrich, France
Glass beads #2	OTS-Store, Germany
Glass beads #3	OTS-Store, Germany
Glass beads #4	OTS-Store, Germany
Glass beads #5	OTS-Store, Germany

Polycaprolactone (PCL average Mw 14'000) was obtained from Sigma Aldrich, France. Dowsil 7091, SYLGARD™ 567 and SYLGARD™ 577 were purchased from Dow Corning (USA). AMSil™ 20101 and LSR 4350 were kindly given by Elkem Silicones, France.

10

Methods

S1. Characterizing powder according to Dynamic Molding

15

Mean diameter (D50)

The particle size distribution was obtained with the use of Mastersizer 2000 coupling with the dry dispersion accessory Scirocco 2000 (Malvern Instruments, UK).

Light from a laser is shone on a cloud of particles, which are suspended in a dispersant (in this study: air). The particles scatter the light, the larger the particles the smaller the scattering angles.

20

The scattered light is measured by a series of photodetectors placed at different angles. This is

known as the diffraction pattern for the sample. The diffraction pattern can be used to measure the size of the particles using Mie or Fraunhofer theory. Obtained results allow to draw a curve, called particle size distribution (volumic distribution), and to calculate parameters such as mean diameter D50.

Compressibility

The compressibility is defined as the reduction of volume according to an applied pressure. Here, the compressibility was evaluated with a rheometer DHR2 (TA instruments, USA) in compression mode and the use of Peltier Concentric Cylinder Temperature System and its standard cup, then a top geometry of 25 mm as diameter. A 20 ml powder sample was included in a Falcon 50 ml tube then placed in Peltier concentric cylinder at 21°C. The measurement procedure involved two steps:

- Step 1: Touching powder surface to define a similar starting point for each powder sample. Top geometry goes down at a speed of 100 µm/s with a stop limit of 0.1 N.
- Step 2: The distance vs force graph was obtained at a compression speed of 10 µm/s up to an applied force of 40 N.

The compressibility in mm/N was defined as the slope of distance/force graph (step 2) through linear regression on TRIOS software (TA Instruments, USA).

S2. Simulation of the Dynamic Molding process

In order to study the behavior of the deposited material in details, the decision has been made to simulate the product injection at the grain level. This is achieved using Computational Fluid Dynamics (CFD) simulations with advanced models. First, a free surface method is used to simulate the moving interface between the deposited material and air. There are two main methods to compute the free surface: the interface tracking method and the front capturing method. The former treats the free surface as a sharp interface whose motion is followed by moving the grid defining the free surface. The latter, commonly used, is performed on a fixed grid and the shape of the interface is determined by the volume fraction of each fluid in the cells. In our case, the front capturing method has been used based on a volume of fluid method (“VOF”). The “VOF” method is a two-phase surface compression method that solves the Navier-Stokes equations and a transport equation for the volume fraction:

$$\frac{\partial c}{\partial t} + \vec{v} \cdot (c\vec{u}) = 0$$

Where c is the volume fraction: $c = 1$ in pure material, $c = 0$ in pure air.

The Modified HRIC method from Peric (1) introduced in ANSYS-Fluent (2) is applied to solve the equation (1) by limiting the numerical diffusion to keep a sharp interface and avoid smearing. The equations are solved using a Pressure Based Coupled Solver (2). The specific viscosity of the deposited materials is taken in account. Here, two different materials respectively described by a Power-law (PL) and Herschel-Bulkley model (HBM) have been tested. In both case surface tension effects are computed with the “CSF” model (for Continuum Surface Force). Moreover, in order to simulate deposition process, a dynamic mesh is used to move the needle over the grains based on sliding mesh [2] with an interface between fixed and moving mesh zones. The interface is non-conformal and ensure flow from the moving to the static part.

S3. Dynamic molding printer modifications

Two DMD printers were used in the present study, each derived from existing systems. The first one, a 3-axis system, was designed on a T333 TOBECA (France) 3D printer. The modifications of the initial printer were:

- Addition of a 20 L heating powder bath instead of the building plate. Heating was obtained through the use of 2x1000 W heating coiled directly connected and controlled by the 3D printer interface.
- Interfacing of a liquid dispensing system (mono or bi component) from ViscoTec (Germany). Special holder were designed and produced through 3D printing (ObjetPro, Stratasys, USA). Stepper motor driver were used to interface the microdosing system with the G-code.
- Interfacing of an air pressure controller (Ultimus™ V, Nordson EFD, USA) through a dedicated electronic board so that the extrusion coded ion the G-code can be translated in pressure delivery information.

The second one, was modified from a 6-axis robotic system (BioAssemblyBot®, Advanced Lifescience Solutions, USA). The modifications of the initial printer were:

- Addition of a 20L heating powder bath instead of the building plate. Heating was obtained through the use of 2x1000W heating coiled directly connected and controlled by the 3D printer interface.
- A special 30CC syringe holder was designed in order to cope with the poor resistance of the initial holder dedicated to 3D printing in non-granular environment. The additional part to the initial holder (STL downloadable at https://github.com/FabricAdvancedBiology/Bioprinter_parts) was 3D printed using an Original Prusa (Prusa3D, Poland).
- For DMD experiments, the BioAssemblyBot® was customized to accommodate printing in the dynamic mold, outside the initial enclosure. To do so, a special safety enclosure was designed which enable the secure operation of the robotic arm while reaching the much larger arena created at the back side of the machine.



Figure S1. The updated BioAssemblyBot® with DMD capability.

S4. Printing protocol using DMD

Printing silicone with Cartesian DMD printer:

- STL files were loaded into Symplify3D® software and sliced using 100 µm height and 200 µm wide deposited filament dimensions. G-code was saved and open by Repetier-Host software, driving the printer movements.
- 30CC cartridge (Nordson EFD, USA) was loaded with monocomponent room temperature vulcanization alkoxy silicone (AMSil™ 20101, Elkem Silicones, France).
- ViscoTec monocomponent microextrusion head (vipro-HEAD 5) was connected to the 30CC cartridge and the feeding pressure set to 4 bars.
- The vipro-HEAD 5 was then equipped with a 200 µm diameter conical nozzle (Nordson EFD, USA) and immersed in the dynamic mold. Deepness of immersion was always between 40 and 80 mm.
- The material dynamic molding was then started at a speed rate of at least 20 mm/s.
- Once the printing completed, a 2 hours material reticulation was performed before taking the printed parts out of the mold.

Printing silicone with 6-axis DMD printer:

- STL files were loaded into TSIM™ software (Advanced Lifescience Solutions, USA) and sliced using 200 µm height and 200 µm wide deposited filament dimensions.
- 30CC cartridge (Nordson EFD, USA) was loaded with monocomponent room temperature vulcanization alkoxy silicone (AMSil™ 20101, Elkem Silicones, France), installed in the DMD special holder and connected to the BioAssemblyBot® pressure controller. The printing pressure was here 4.8 bars.
- The 30CC cartridge head was then equipped with a 200 µm diameter conical nozzle (Nordson EFD, USA) and immersed in the dynamic mold. Deepness of immersion was always between 40 and 80 mm.
- The material dynamic molding was then started at a speed rate of 10 mm.sec⁻¹.
- Once the printing completed, a 2 hours material reticulation was performed before taking the printed parts out of the mold.

Printing PCL with 6-axis DMD printer:

- STL files were loaded into TSIM™ software (Advanced Lifescience Solutions, USA) and sliced using 200 µm height and 200 µm wide deposited filament dimensions.
- 30CC high temperature cartridge (Nordson EFD, USA) was loaded with polycaprolactone (average Mw 14'000, Aldrich, France), installed in the BioAssemblyBot® heating holder and connected to the BioAssemblyBot® pressure controller. The printing pressure was here 0.7 bars and the head temperature 90°C.
- The 30CC cartridge heating head was then equipped with a 200 µm diameter metallic conical nozzle (FISNAR, France) and immersed in the dynamic mold. Deepness of immersion was always between 40 and 80 mm and the mold temperature set to 100°C.
- The material dynamic molding was then started at a speed rate of 10 mm/s.
- Once the printing completed, a 12 hours material cool down was performed before taking the printed parts out of the mold.

S5. Post-processing

When printing using dynamic molds, powder residues are present at the surface or within the material composing of the obtained objects. A post-treatment can then be applied to remove these residues.

For non-sacrificial powder (silica, glass or cenosphere for example), a high pressure water cleaner was used once the printed material fully reticulated.

For PMMA sacrificial material, once the printed material fully reticulated, the parts were immersed in acetone for 2 hours, then rinsed with ethanol for an additional 2 hours and air dried.

S6. Mechanical properties characterization

Dumbbell-shaped printed samples of H2 form of the NF EN ISO 527-1 were used to measure the Young's modulus (E) and fracture strain. A CRITERION (MTS Systems, Créteil, France) tensile testing machine equipped with a 500-N load cell was used to perform the uniaxial tensile tests.

Young's modulus of each samples was obtained from the following equation using the true stress (σ) and the true strain (ε) between 0 to 10%. The fracture strain was defined as the true strain when the printed H2 form was broken.

$$E_{0 \rightarrow 10\%} = \frac{\sigma}{\varepsilon} = \frac{F * L}{e * l * L_0 \ln\left(\frac{L}{L_0}\right)}$$

Where L_0 is the initial length, L the displacement, F the force, e the thickness and l the width.

S7. Electronic microscopy

Scanning electron microscopy imaging was performed using a Merlin Compact (Zeiss) at the *Centre Technologique des Microstructure* (Université Lyon1, France).

S8. Silicone elastomer viscosity measurements

Rheology measurements were conducted using a stress-controlled Discovery HR-2 rheometer (TA Instruments, USA) with a plate-plate geometry of 40 mm in diameter. Characterization was performed just after mixing and degassing. Flow sweep procedure with 5 pts/decade was performed between 0.01 to 10 s^{-1} , to establish the viscosity vs shear rate and shear stress vs shear rate relationships. First, viscosity value was defined at 0.01 s^{-1} (low shear rate, near to the rest). Then, static yield stress was extracted from Hershel-Bulkey model (see equation below) available with TRIOS software (TA instruments, USA) to implement the FingerMap predictive tool

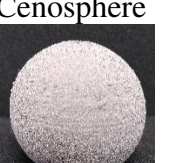
$$\tau = \tau_y^s + k\dot{\gamma}^n$$

Where τ is the shear stress, τ_y^s the shear static shear stress, $\dot{\gamma}$ the shear rate, k the consistency index and n the flow index.

Supplementary Text

S9. Deposition elastomer material properties and dynamic molding

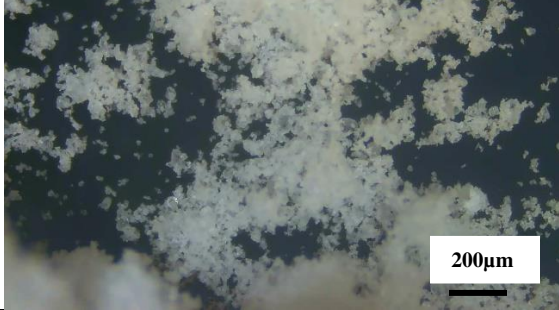
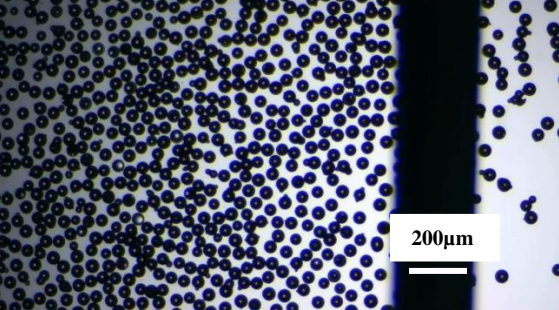
5 **Table S2.** Properties of the elastomers used in the present study together with examples of 2 cm diameter printed objects.

Material	Viscosity (shear rate fixed at 10^{-1} s^{-1})	Static yield stress (Pa)	Pot life	DMD mold and object obtained
SYLGARD™ 567, Dow Corning	$2 \times 10^1 \text{ Pa}\cdot\text{s}$	0.94	24 hours	Glass 
SYLGARD™ 577, Dow Corning	$7 \times 10^1 \text{ Pa}\cdot\text{s}$	0.00	22 hours	Glass 
AMSil™ 20101, Elkem Silicones	$3 \times 10^3 \text{ Pa}\cdot\text{s}$	6×10^2	10 minutes (skin)	Glass 
LSR 4350, Elkem Silicones, France	$5 \times 10^3 \text{ Pa}\cdot\text{s}$	3×10^2	>24 hours	Cenosphere 
Dowsil 7091, Dow Corning	$10^4 \text{ Pa}\cdot\text{s}$	3.5×10^2	15 minutes (skin)	Silica 

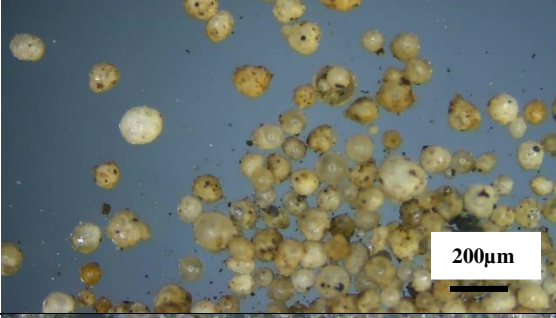
S10. Powder characterization full data

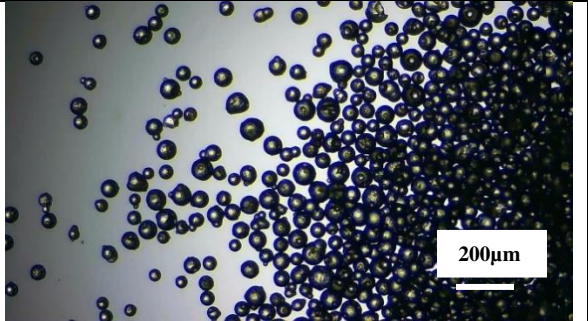
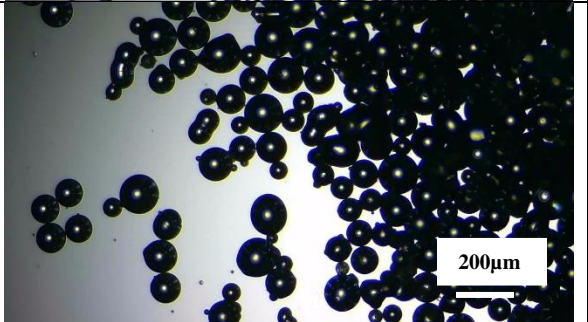
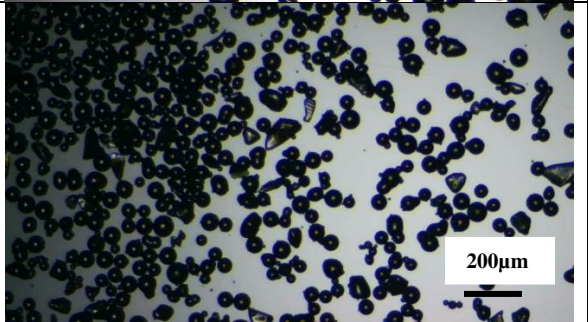
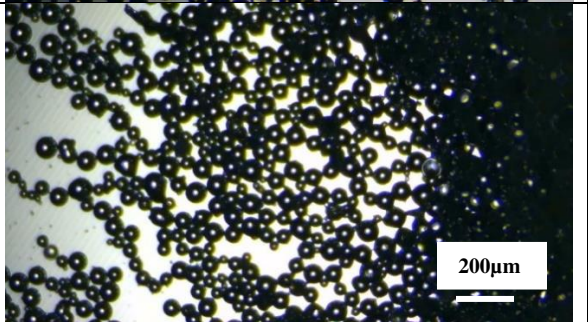
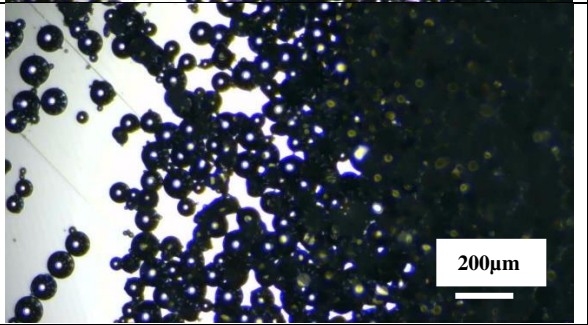
Table S3. Properties of the powder used in the present.

5

DMD powder	Particles mean size (μm)	Compressibility (mm/N)	Image
Cement	12	359.70	
Icing sugar	61	333.83	
Flour	72	263.15	
Glass beads #1	55	17.88	

Cornflour	13	232.80	
Laundry powder	320	157.95	
Ground coffee (small)	115	82.80	
Ground coffee (coarse)	1200	73.95	
Sugar	451	67.60	

Sand	431	43.80	 <p>Micrograph showing irregular, light-colored sand particles of various sizes against a dark background. A scale bar in the bottom right corner indicates 200µm.</p>
Cenosphere	107	41.15	 <p>Micrograph showing spherical, light-colored cenosphere particles of various sizes against a dark background. A scale bar in the bottom right corner indicates 200µm.</p>
PMMA	91	32.25	 <p>Micrograph showing numerous small, spherical, light-colored PMMA particles against a dark background. A scale bar in the bottom right corner indicates 200µm.</p>
Bicarbonate	165	29.33	 <p>Micrograph showing irregular, light-colored bicarbonate particles of various sizes against a dark background. A scale bar in the bottom right corner indicates 200µm.</p>
Fine salt	1200	27.98	 <p>Micrograph showing large, irregular, light-colored fine salt particles against a dark background. A scale bar in the bottom right corner indicates 200µm.</p>

Silica beads	102	15.08	
Glass beads #2	150	12.13	
Glass beads #3	90	16.63	
Glass beads #4	125	15.65	
Glass beads #5	150	45.85	

S11. Simulation

The resulting simulations for the two different fluids are presented in **Figure S2** and **Movie S1** and **Movie S2**. One can see the influence of material property on deposition process. These information are valuable to understand and improve deposition process.

Here, according to the material viscosity (see **Table S2**), inter-particles flow of the material was demonstrated, leading to the production of highly charged composites.

Movie S1: simulations of SYLGARD™ 567 deposition in glass beads dynamic mold

Movie S2: simulations of AMSil™ 20101 deposition in glass beads dynamic mold

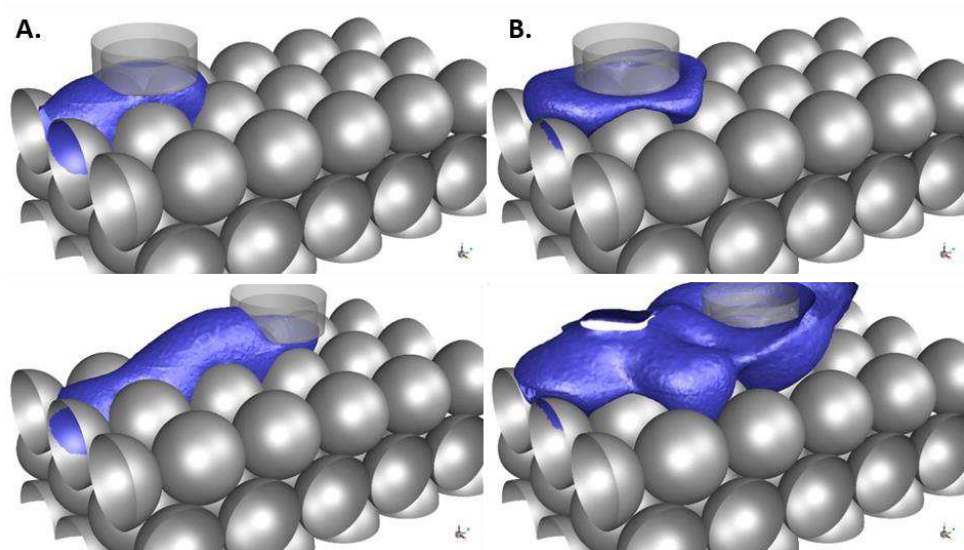


Figure S2: Simulation of the interaction of the deposited material with the dynamic mold.
A. Deposition of SYLGARD™ 567 deposition in glass beads dynamic mold. B. AMSil™ 20101 deposition in glass beads dynamic mold

5

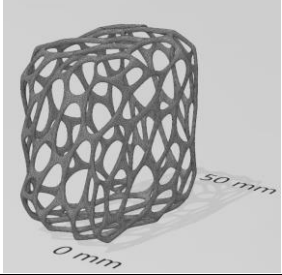
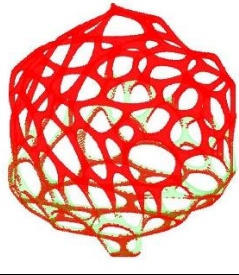
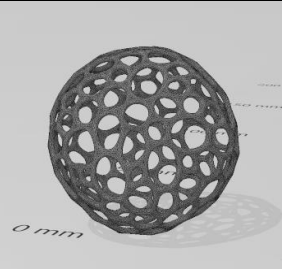
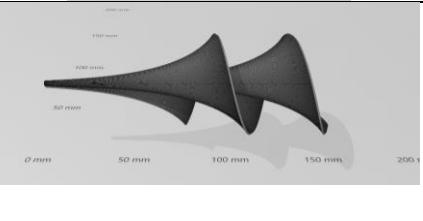
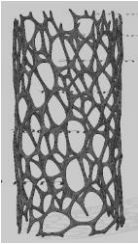
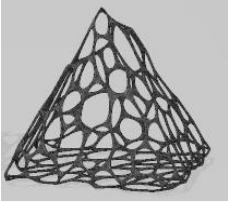
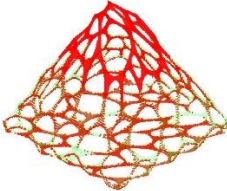
S12. FingerMap of the different printed objects (3)

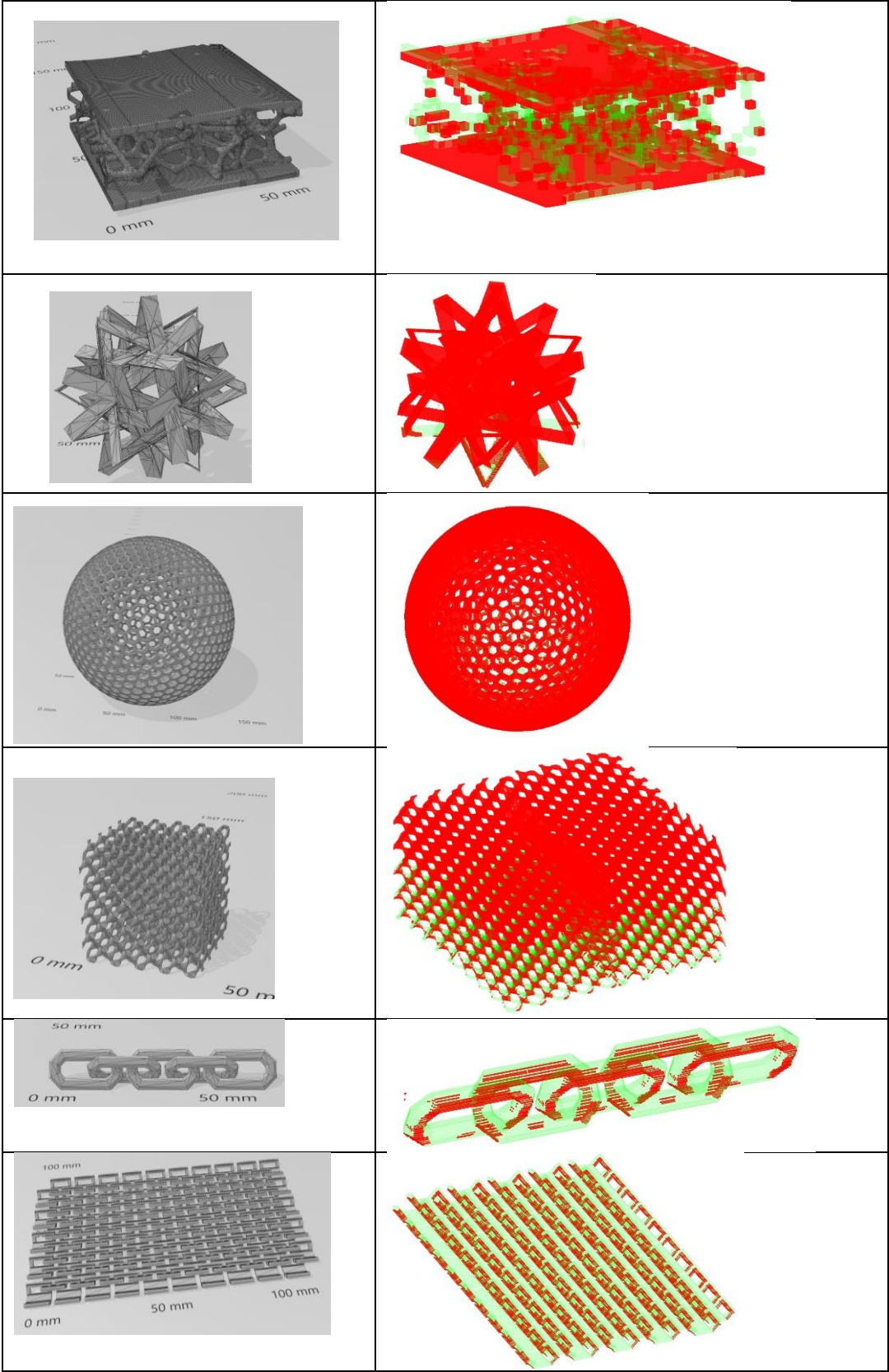
5 A custom MATLAB (MathWorks® R2018B, USA) code was used. The code uses an STL file as an input and indicates troublesome areas to print on the basis of the measured τ_y^s and the known formulation density. To briefly resume, the code first voxelizes the STL file (each point of the object volume being represented by a voxel), then treats each voxel to determine its carried mass, detects its overhanging status and determines its overhanging angle value. From this voxelization, the Fingermap of the 3D object can be built. The prediction level is given when the FingerMap is compared to the printability volume as a function of material rheological properties. The voxel displays as red if the τ_y^s is not high enough to withstand the shape complexity. Otherwise, the voxel displays as green.

10

Table S4. Printability of the different objects simulated using the FingerMap program. The voxel displays as red if the τ_y^s is not high enough to withstand the shape complexity. Otherwise, the voxel displays as green.

5

STL file	FingerMap
	
	
	
	
	



S13. Lattice structure printing in 6-axis

In **Movie S3** and **Movie S4**, an AMSil™ 20101 silicone complex lattice molded in glass bead using a 6-axis system is shown.

5

S14. Softness of the obtained material

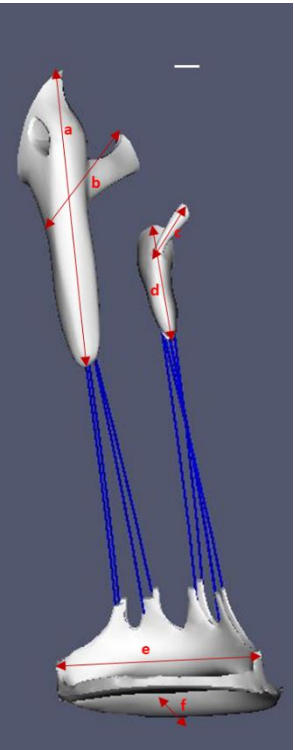
- 5 In **Movie S5**, the extension capability of an AMSil™ 20101 silicone complex textile molded in glass bead is shown.
In **Movie S6**, the compressibility capability of a SYLGARD™ 567 silicone ball molded in PMMA is shown.

10 S15. Multiple material object

In **Movie S7**, the multimaterial AMSil™ 20101 silicone voroid sphere molded in glass bead is shown.

S16. Dimensional analysis of the highly complex physiological shape composed of a mitral valve, eight chordae tendineae and two medial papillary muscles

5 **Table S5.** Fidelity study of the complex physiological parts. Measured were performed with an electronic caliper.

	Muscle				Valve	
	a	b	c	d	e	f
						
Mean measured dimensions (mm)	81.09	32.00	15.77	32.44	63.11	57.41
STL Values (mm)	82.22	33.32	16.19	32.01	60.47	56.61
Difference (mm)	1.13	1.32	0.42	0.43	2.64	0.80
Difference (%)	1.37	3.96	2.59	1.34	4.37	1.41
Mean difference per part (mm)	0.96			1.29		
Print fidelity per part (%)	97.36			97.63		
Overall mean difference (mm)	1.12					
Overall print fidelity (%)	97.49					

S16. DMD resolution estimation

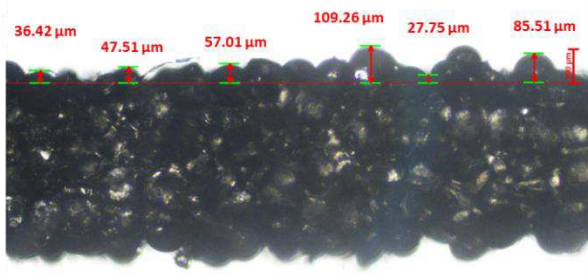
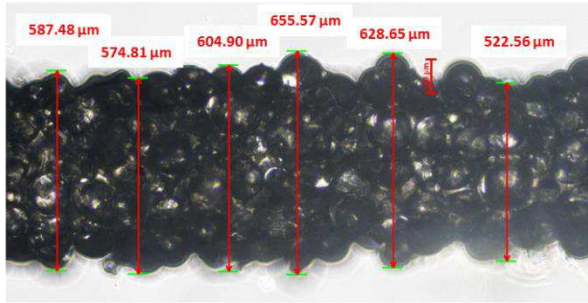
5 DMD resolution was estimated through the dynamic molding of 400 μm thick and 2 cm high thin silicone membrane in glass beads #4. Then, thin cuts of the object were performed, parallel or perpendicular to the filament deposition, and the thickness of the membrane estimated from microscopy images (**Figure S3**).

10 As can be seen, the final thickness of the object was 595 μm or 552 μm , depending of the cut direction. These values correspond to the size of the injected silicone, i.e. 400 μm , plus 2-times the mean roughness given by the glass beads (60 μm).

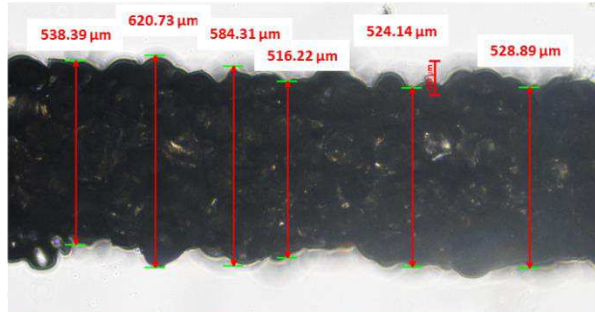
15 Interestingly, low variation coefficients were found for the object thickness (7-8%), corresponding to a standard deviation of 41-46 μm .

Finally, out of these measurements, a mean resolution (the largest obtained roughness) of 100 μm can be estimated.

Cut perpendicular to filament direction



Cut parallel to filament direction



	Thickness Perpendicular (μm)	Thickness Parallel (μm)	Roughness Perpendicular (μm)
	587.48	538.39	36.42
	574.81	620.73	47.51
	604.90	584.31	57.01
	655.57	516.22	108.26
	628.65	525.14	27.75
	522.56	528.89	85.51
Mean (μm)	595.66	552.28	60.41
Standard deviation	46.06	41.20	30.79
Variation coefficient (%)	7.73	7.46	50.97

Figure S3. Microscopy images of cuts of a 400μm thick silicone membrane produced in a glass beads mold.

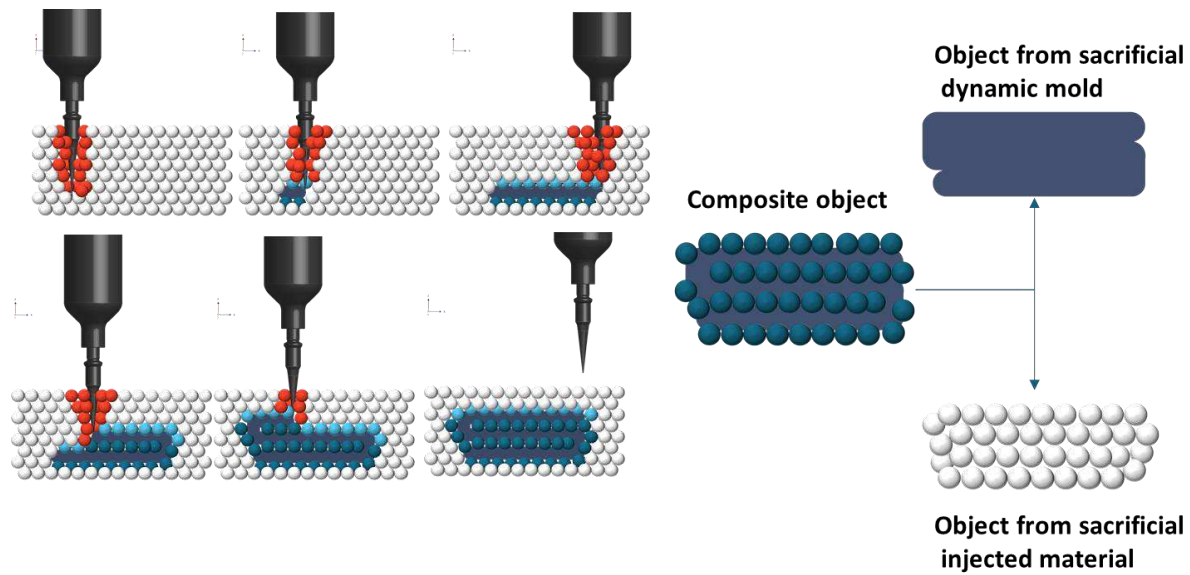


Figure S4. Conceptual approach of the DMD showing the alternative process in which composite is produced and shall lead to three different type of objects.

5

References and Notes:

1. M. Peric, J. H. Ferziger, *Computational method for fluid dynamics*. (Springer, ed. 3rd 2002).
2. in *ANSYS Fluent Theory Guide*. (ANSYS, Inc. , Release 2020 R2).
3. A. Lopez, C. A. Marquette, E.-J. Courtial, FingerMap: a new approach to predict soft material 3D objects printability. *Progress in Additive Manufacturing* **6**, 53 (2021/02/01, 2021).

10

15

Figures

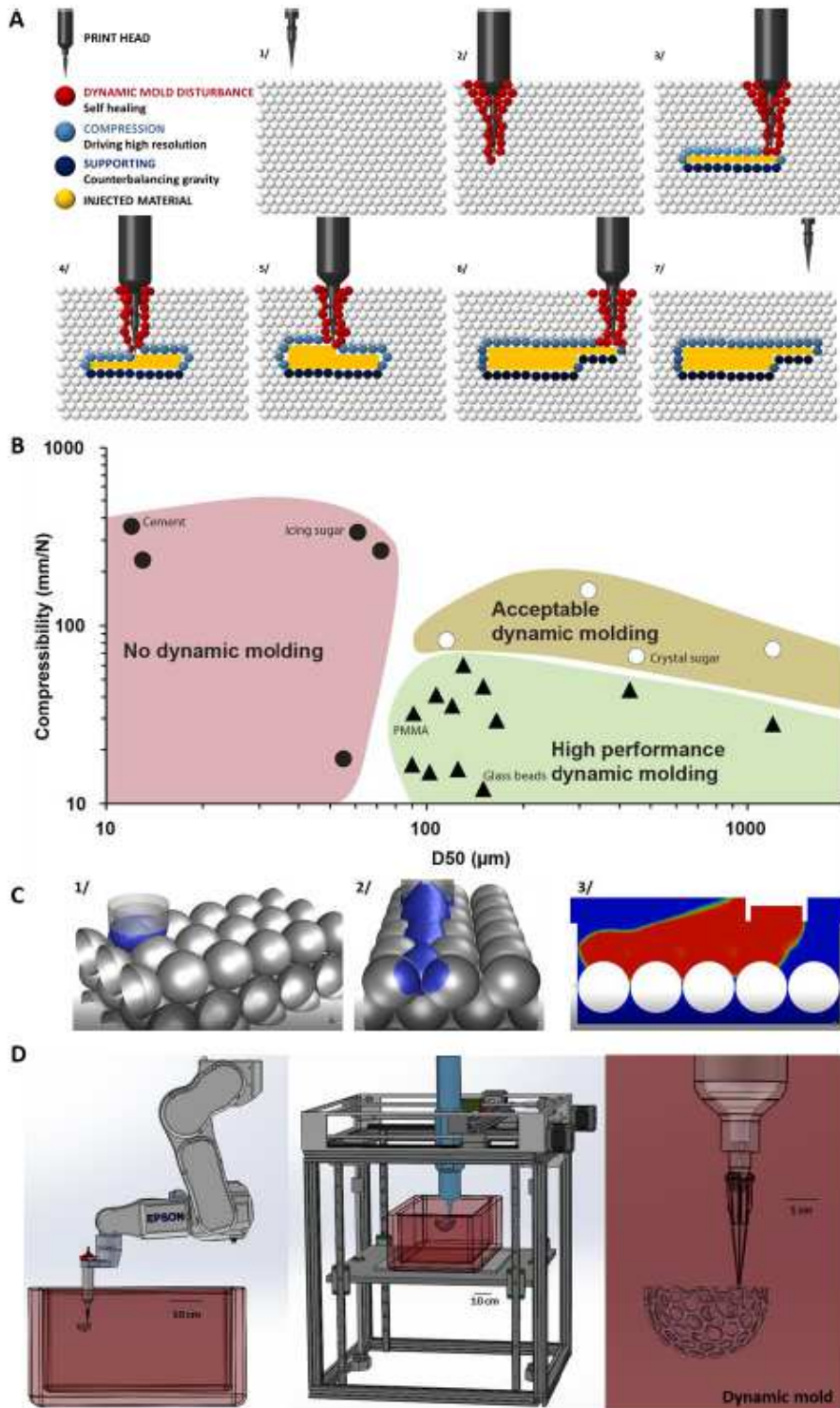


Figure 1

Dynamic Molding Deposition. (A) Conceptual approach of the DMD showing the different behaviors of the dynamic mold (composite variant process can be found in Figure S4). Material printing sequence of two layers, from 1/ to 7/. (B) Selection mapping of the dynamic mold according to compressibility and

particle diameter. (C) Computational Fluid Dynamics (CFD) modelling simulation of SYLGARD™ 567 DMD within silica beads. 1/ at t=0, 2/ at t= 8.5 msec, 3/ profile of the deposited material. (D) Modified 3D printers, 6-axis robotic (left) and 3-axis printer (center). Closer view of the DMD of a voroid sphere without building plate or support structure.

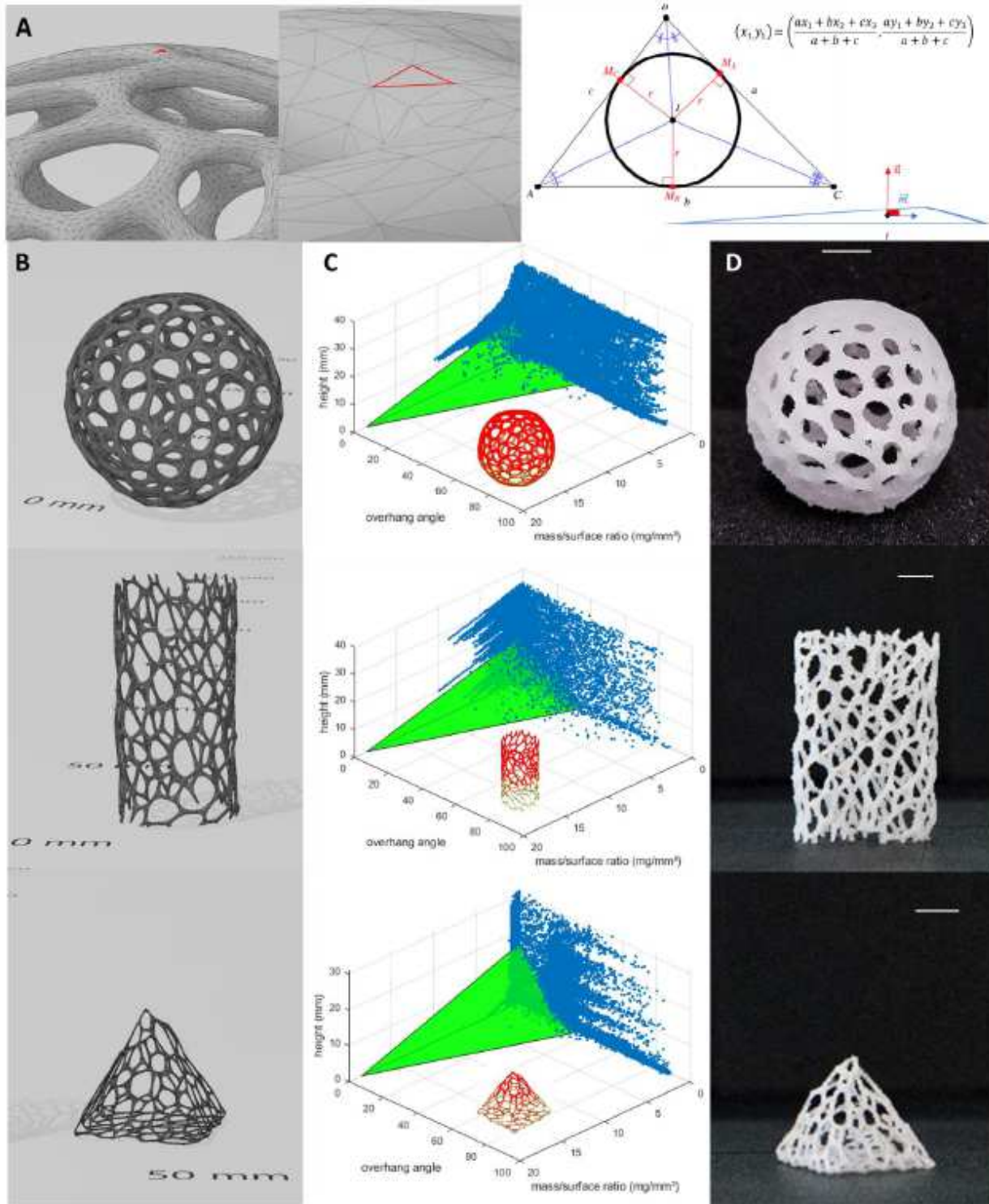
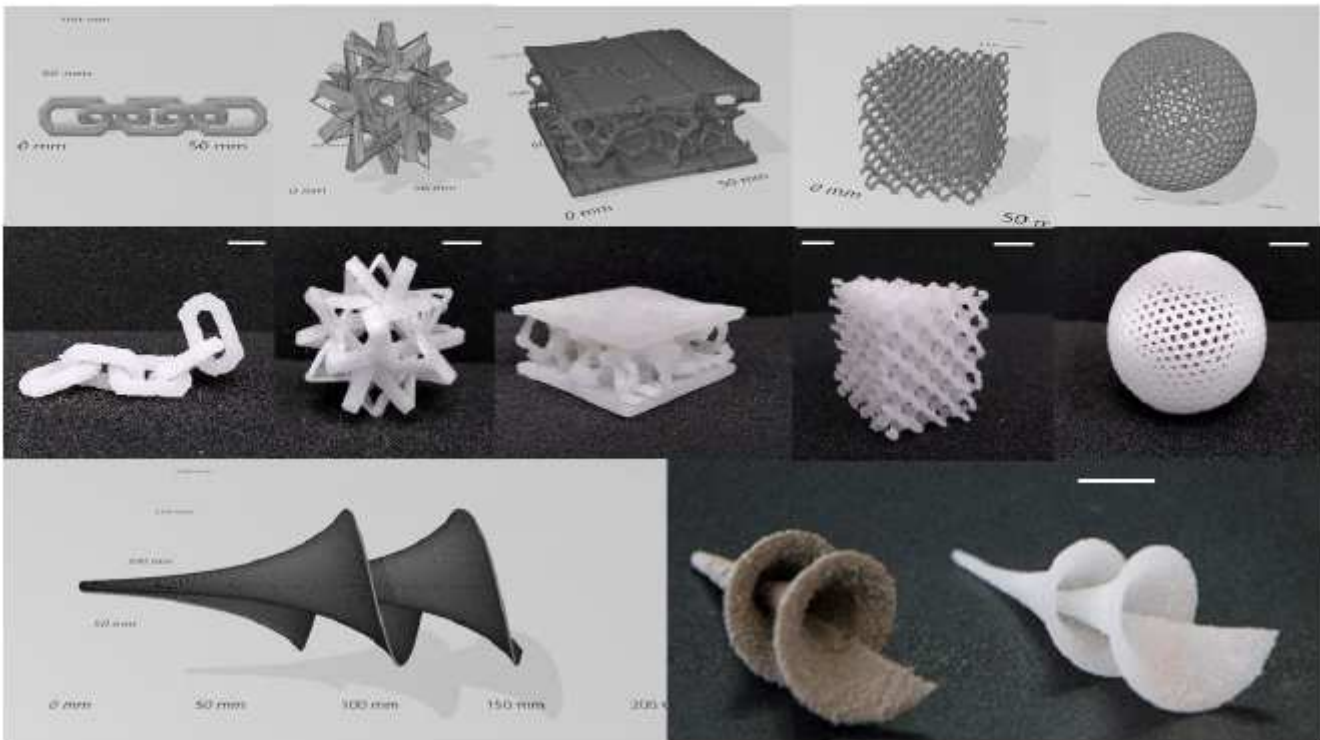


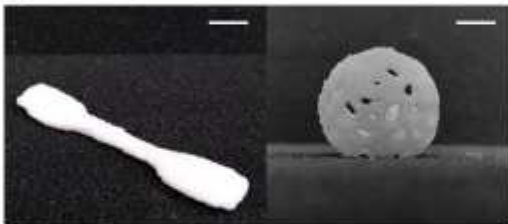
Figure 2

voids printability simulation using FingerMap. (A) Each triangle of STL file is described through incenter by FingerMap tool. The incenter I is the center of the incircle for a polygon or insphere for a polyhedron. For a triangle with Cartesian vertices (x_1, y_1) , (x_2, y_2) , (x_3, y_3) , the Cartesian coordinates of the incenter are given by the presented equation. Then, normal vector (red) is defined for each triangle of STL file from incenter corresponding to $\vec{n} \cdot \vec{r} = 0$. (B) STL file of the studied voroids. (C) FingerMap and simulation and the experimental 3D print (insert) for each STL. The green volume represents the printability of the material. Each blue dot represents a voxel. In the prediction, red voxels represent not-printable area while green voxels represent printable area. (D) Voroids obtained through DMD using monocomponent room temperature vulcanization alkoxy silicone (AMSil™ 20101) within glass beads.

A



B



C



D



Figure 3

Multiple examples of complex objects produced by DMD. (A) A series of highly complex STL geometries (top) and produced objects (bottom) obtained using monocomponent room temperature vulcanization alkoxy silicone (AMSil™ 20101) within glass beads (white parts) or cenospheres (grey parts) dynamic molds. (B) Polycaprolactone thermoplastic H2 tensile bar and voroid sphere obtained using DMD in glass beads. (C) Voroid ball within voroid ball STL (left) and object produced using two colored alkoxy silicone (AMSil™ 20101). (D) DMD enabling production of complex shapes through the merging of 3-axis and 6-axis multidirectional deposition within a single object. Left: STL multiple files and multidirectional trajectories (blue lines). Center: the DMD enabled object. Right: a closer view of the cohesion between Cartesian print and multidirectional deposition. Scale bars are 1 cm.

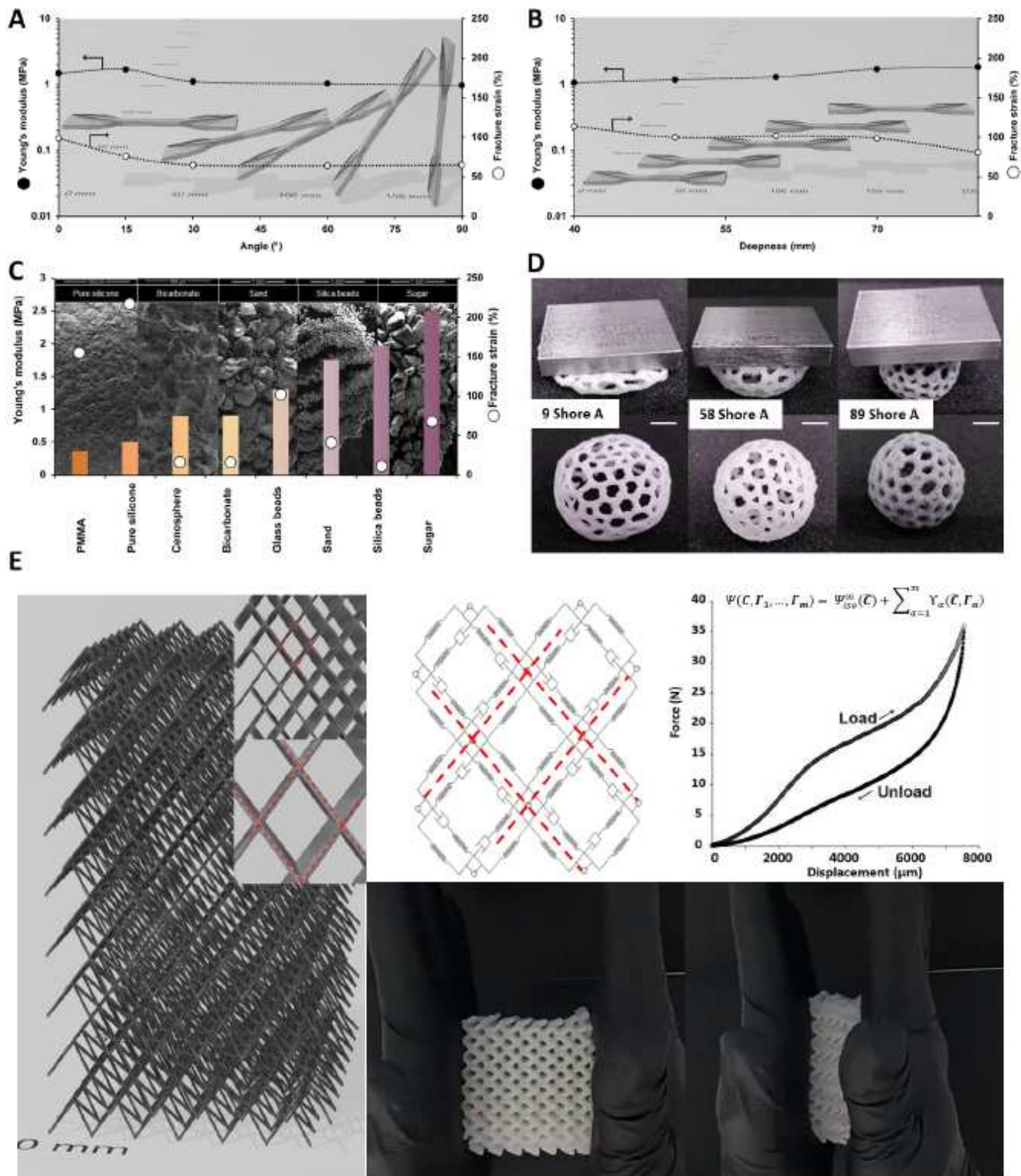


Figure 4

DMD produced objects and composites characterizations. (A) Mechanical properties (Young's modulus and Fracture strain) of DMD silicone objects positioned at different angles within a single glass beads mold (mean error for all measurements 5%). (B) Mechanical properties (Young's modulus and Fracture strain) of DMD silicone objects positioned at different deepness within a single glass beads mold (mean error for all measurements 5%). (C) Topographic analysis (electronic microscopy images in background)

and mechanical properties (Young's modulus and Fracture strain) of multiple silicone (AMSil™ 20101) composites (mean error for all measurements 5%). (D) Demonstration of the capacity of the DMD to produce a wide range of stiffness (testing weight: 50g). Left: AMSil™ 20101 obtained in sacrificial PMMA powder. Center: AMSil™ 20101 obtained in glass beads powder. Right: SYLGARD™ 567 obtained in glass beads powder. (E) Lattice structure characterized by a non-linear hyper-viscoelastic behavior and obtained using path-based 6-axis deposition strategy. Mechanical model representative of the non-linear hyper-viscoelastic. Load/unload compression curve and constitutive equation.

Supplementary Files

This is a list of supplementary files associated with this preprint. Click to download.

- [MovieS1SYLGARDXXX567.mp4](#)
- [MovieS2AMSilXXX20101.mp4](#)
- [MovieS3.mp4](#)
- [MovieS6.mp4](#)
- [MovieS7.mp4](#)
- [MovieS4.mp4](#)
- [MovieS5.mp4](#)